A joint numerical study of multi-regime turbulent combustion

Benoit Fiorina, Tan Phong Luu, Samuel Dillon, Renaud Mercier, Ping Wang, Lorenzo Angelilli, Pietro Paolo Ciottoli, Mauro Valorani, Hong G Im, James C Massey, et al.

A joint numerical study of multi-regime turbulent combustion

Benoît Fiorina[a,], Tan Phong Luu[a], Samuel Dillon[a,b], Renaud Mercier[b], Ping Wang[c], Lorenzo Angelilli[d], Pietro Paolo Ciottoli[e], Francisco E. Hernández-Pérez[d], Mauro Valorani[e], Hong G. Im[d], James C. Massey[f,g], Zhiyi Li[f], Zhi X. Chen[h], Nedunchezhian Swaminathan[f], Sebastian Popp[i], Sandra Hartl[i], Hendrik Nicolai[i], Christian Hasse[i], Andreas Dreizler[i], David Butz[i], Dirk Geyer[j], Adrian Breicher[j,i], Kai Zhang[k], Christophe Duwig[k], Weijie Zhang[l], Wang Han[m], Jeroen van Oijen[n], Arthur Péquin[o], Alessandro Parente[o], Linus Engelmann[p], Andreas Kempf[p], Maximilian Hansinger[q], Michael Pfitzner[q], Robert S. Barlow[r,i]

[a] *Université Paris-Saclay, CNRS, CentraleSupélec, Laboratoire EM2C, 91190, Gif-sur-Yvette, France*
[b] *SAFRAN Tech, Digital Sciences & Technologies Department, Rue des Jeunes Bois, Châteaufort, 78114 Magny-Les-Hameaux, France*
[c] *Institute for Energy Research, Jiangsu University, China*
[d] *King Abdullah University of Science and Technology, Saudi Arabia*
[e] *Sapienza University of Rome, Italia*
[f] *Department of Engineering, University of Cambridge, Trumpington Street, Cambridge CB2 1PZ, United Kingdom*
[g] *Robinson College, University of Cambridge, Grange Road, Cambridge CB3 9AN, United Kingdom*
[h] *State Key Laboratory of Turbulence and Complex Systems, Aeronautics and Astronautics, College of Engineering, Peking University, Beijing 100871, China*
[i] *Technical University of Darmstadt, Germany*
[j] *Darmstadt University of Applied Sciences, Germany*
[k] *KTH, Royal Institute of Technology, Sweden*
[l] *Xi'an Jiaotong University, China*
[m] *Beihang University, China*
[n] *Eindhoven University of Technology, The Netherlands*
[o] *Université Libre de Bruxelles, Belgium*
[p] *University of Duisburg-Essen*
[q] *Universität der Bundeswehr München, Germany*
[r] *Barlow Combustion Research, CA, USA*

Email address: benoit.fiorina@centralesupelec.fr (Benoît Fiorina)

Preprint submitted to Applications in Energy and Combustion Science November 3, 2023

Abstract

This article presents a joint numerical study on the Multi Regime Burner configuration. The burner design consists of three concentric inlet streams, which can be operated independently with different equivalence ratios, allowing the operation of stratified flames characterized by different combustion regimes, including premixed, non-premixed, and multi-regime flame zones. Simulations were performed on three LES solvers based on different numerical methods. Combustion kinetics were simplified by using tabulated or reduced chemistry methods. Finally, different turbulent combustion modeling strategies were employed, covering geometrical, statistical, and reactor based approaches. Due to this significant scattering of simulation parameters, a conclusion on specific combustion model performance is impossible. However, with ten numerical groups involved in the numerical simulations, a rough statistical analysis is conducted: the average and the standard deviation of the numerical simulation are computed and compared against experiments. This joint numerical study is therefore a partial illustration of the community's ability to model turbulent combustion. This exercise gives the average performance of current simulations and identifies physical phenomena not well captured today by most modeling strategies. Detailed comparisons between experimental and numerical data along radial profiles taken at different axial positions showed that the temperature field is fairly well captured up to 60 mm from the burner exit. The comparison reveals, however, significant discrepancies regarding CO mass fraction prediction. Three causes may explain this phenomenon. The first reason is the higher sensitivity of carbon monoxide to the simplification of detailed chemistry, especially

when multiple combustion regimes are encountered. The second is the bias introduced by artificial thickening, which overestimates the species' mass production rate. This behavior has been illustrated by manufacturing mean thickened turbulent flame brush from a random displacement of 1-D laminar flame solutions. The last one is the influence of the subgrid-scale flame wrinkling on the filtered chemical flame structure, which may be challenging to model.
Keywords:
Turbulent Combustion Modeling, Large Eddy Simulation, Pollutant formation, Model comparison, Multi regime combustion

---

1. Introduction

Most novel combustion chambers promote stratified combustion regimes to limit the flame temperature while ensuring the flame stabilization [1]. In terms of turbulent combustion modeling, challenges are to handle multiple combustion regimes which differ from canonical models usually dedicated to either premixed or non-premixed flame structures [2].

A numerical combustion strategy results from modeling choices made at two levels, corresponding to chemistry simplification and turbulent combustion modeling. Indeed, because of the complexity of combustion chemistry, detailed chemical schemes must be first simplified before being implemented into a CFD solver. Three major routes, namely *reduced*, *tabulated* and *optimized* chemistry have been proposed to describe kinetic effects at a reduced computational cost [3]. *Reduced* chemistry aims to decrease the number of reactions and species involved in a detailed kinetic scheme by removing species and reactions that will not significantly affect targeted flame properties [4, 5]. Further reduction of the kinetics can be achieved to find analytical relations between species by applying, for instance, a Quasi-Steady State Approximation (QSSA) [6, 7]. *Tabulated chemistry* aims to express the thermochemical variables in a reduced chemical state space prior to a CFD computation [8]. Key issues of tabulated chemistry techniques are the generation of the chemical look-up table and the choice of coordinates. Because of their ease of implementation and low cost, flamelet-based tabulated chemistry methods are very popular for engineering applications [9]. However, the definition of the tabulated flamelet archetype, in general either premixed [10, 11] or non-premixed [12, 13], potentially limits the range of validity of the method

to a single combustion regime [14]. Finally, *optimized* chemistry aims at generating small mechanisms (from 1 to 4 steps in general), whose kinetic rate parameters are optimized to capture global flame properties such as, for example, the burning velocity and flame temperature [15, 16] but also pollutant formation [17].

Once the chemistry is simplified, there are also three main alternatives to model turbulent combustion, which are the *geometrical*, *statistical* or *reactor based* approaches [18]. *Geometrical* methods, which model the flame front by a surface wrinkled by the turbulence, are designed to capture the flame front propagation in premixed or stratified combustion regimes. Under resolution of the flame front, whose thickness is in general smaller than the grid size, is generally managed by artificial thickening [19] or filtering [20], while subgrid scale flame wrinkling is modeled [21, 22]. *Statistical* approaches describes the impact of turbulence on thermochemical flame properties by introducing Filtered Density Functions, which can be either transported or presumed [23]. Finally *reactor based* approaches, which assume that combustion occurs at small dissipative scales, are adapted to distributed combustion regimes [24, 25].

The multiple possible combinations of *simplified chemistry* and *turbulent combustion* sub-models as well as the intrinsic differences between the different CFD flow solvers will lead to disparate simulation results. The evaluation of simulation data quality is the main objective of the TNF Workshop [26] where research groups agree to compute well-defined, experimentally characterized, target flames by using different models and codes. Within this framework, five research groups performed Large Eddy Simulations of the

TSF A turbulent stratified flame configuration [27]. Despite the use of different turbulent combustion models and solvers, most simulations agree on the mean flame brush position and on the temperature fields [28]. The impact on the pollutant prediction, was not addressed within that study.

This article presents the results of a new joint numerical study conducted on a novel target flame series stabilized on the Multi Regime Burner (MRB), designed at TU Darmstadt and Darmstadt UAS and measured both in Darmstadt and at Sandia National Laboratories [29]. The burner configuration allows the operation of stratified flames stabilized by the flow field with well defined inflow and boundary conditions, promoting different combustion regimes, including premixed, non-premixed and multi-regime flame zones. In addition to velocity, mixing, and temperature statistics, measurements now include data on the carbon monoxide mass fraction. Recently published simulations performefed of the MRB highlighted the difficulty to predict CO because its formation involves various chemical time scales [29–31].

Ten numerical groups are here involved in the numerical simulations: Technische Universität Darmstadt, University of Cambridge, Université Paris Saclay, KAUST, KTH Royal Institute of Technology, Jiangsu University, Université Libre de Bruxelles, Universität Duisburg Essen, the group of Xi'an Jiaotong University, Beihang University and Eindhoven University of Technology, and Universität der Bundeswehr München. The objective is to partially illustrate the ability of e turbulent combustion modeling community on multi-regime flame simulations. As many numerical and modeling parameters differ among the simulations, this exercise does not allow a fine sub-model comparison. However, it aims to identify the physical phenom-

ena which remain challenging to predict by most of the modeling strategies. Each group decided on its own numerical and modeling strategy, independently of the other simulations, as no specific guidance was given prior to the simulations. The analysis of the results will therefore not allow us to conclude on best practice.. The explanations for the differences observed between the simulations should be considered as scenario suggestions rather than definitive conclusions.

The present work's originality relies on the possibility of showing the average and standard deviation of simulations thanks to the large amount of collected data. Definitive conclusions regarding turbulent combustion model parameters are impossible, as too many parameters change between numerical cases. However, this significant scattering of numerical and modeling strategies is also an advantage as it illustrates the strengths and weaknesses of the state-of-the-art. This exercise is especially interesting to the engineers in charge of the simulation of reactive systems.

The article is organized as follows. The MRB configuration is presented in Sec.2, the different numerical and combustion modeling strategies are given in Sec. 3 and results are shown in Sec.4. The analysis discusses first the ability of the simulations to qualitatively reproduce the flame lift-off. A comparison between simulations and experiments is then conducted for the velocity, the species and the temperature fields in both outer and inner flame regions, characterized by premixed dominant and multiple combustion regimes, respectively. A focus is made on the influence of artificial flame thickening on the CO prediction. Scatter plots of temperature and CO mass fraction are finally analyzed in the mixture fraction space.

2. The Multi Regime Burner configuration

The MRB configuration, designed and experimently studied by Butz *et al.* [29], is made of three concentric inlet streams, each characterized by its own equivalence ratio. A schematic view of the burner geometry is given in Fig. 1. A rich premixed flow of methane and air is injected through the center tube (called "jet"). This main injection stream is surrounded by two concentric annular tubes, called "slot 1" and "slot 2". Pure air is injected through "slot 1", while a lean premixed flow of methane/air characterized by an equivalence ratio of 0.8 is injected through "slot 2". The temperature of the conical bluff body separating "slots 1" and "2" is regulated by water at 80 °C. Finally, a second bluff body separates "slot 2" from a low-speed air co-flow. Two operating conditions are computed here, namely MRB18b and MRB26b, which correspond to a main jet equivalence ratio of 1.8 and 2.6, respectively. For both cases, bulk velocities of the main jet, "slot 1" and "slot 2" streams are equal to 105 m/s, 15 m/s and 20 m/s, respectively. The high shear between the jet and "slot 1" induces fast mixing and the formation of the multi regime characteristics. A non-reactive flow configuration, called COLD, has also been measured under the same operating conditions as MRB18b [32].

Available experimental data include the velocity field measured from PIV [32] and the thermochemical flame structure given by Raman/Rayleigh/CO-LIF diagnostics [29]. From spatially resolved measurements of temperature, mixture fraction, and major species mass fraction, Butz *et al.* [29] analyzed the turbulent flame structure of the inner reaction zone by applying the Gradient Free Identification regime criteria [33]. They mainly reported premixed flame archetypes near the burner exit for both MRB18b and MRB26b. Then,

with increasing axial distance, the flame structure evolves with a growing importance of multi-regime structures, especially for MRB26b. Finally, while premixed flame regions remain dominant for the full length of MRB18b, non-premixed flame structures become significant in the downstream region of MRB26b, also observed numerically [31].

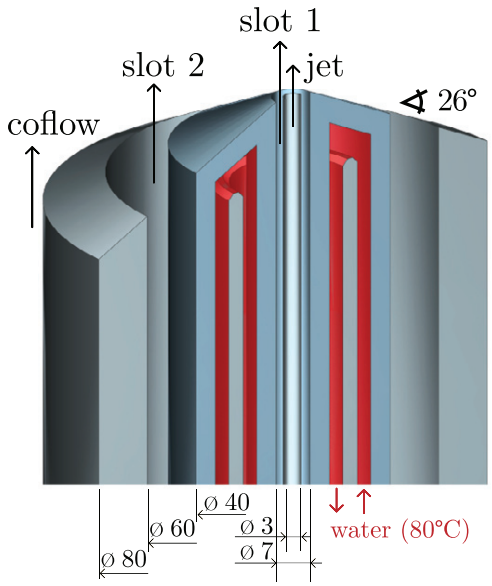

Figure 1: MRB burner geometry, from [29].

3. Numerical and combustion modeling strategies

3.1. Numerical set-up

The composition of the nine numerical and the experimental teams involved in the present study is indicated in Tab. 1 along with the cases computed by each group. The colored text in the first row indicates the color retained to distinguish the curves plotted later for radial profile comparisons.

Table 2 details the corresponding numerical strategies. All groups conducted Large Eddy Simulations, including eight with the OpenFOAM solver and one each using the YALES2 [34] and PsiPhi [35] solvers. Simulations Num A and Num E employ the same grid, designed by TU Darmstadt [30]. Otherwise, a wide range of mesh resolution conditions is covered, with three orders of magnitude between the coarsest and finest grids composed of 1M and 2.2B elements, respectively. Four different models have been used to close the unresolved turbulent fluxes: WALE [36] , K-equation, Sigma [37] and dynamic Smagorinsky [38]. For the given turbulent jet flow, non-reactive flow simulations presented in Supplementary Materials shows that the SGS closure of the filtered momentum equations does not significantly influence the prediction of the aerodynamic field.

3.2. Chemistry simplification

The combustion modeling strategies, given in Tab. 3, combine first a simplification of the detailed kinetics and then a modeling of subgrid scale interactions between the flame and the turbulence. As discussed in [3], simplified chemistry methods fall into three categories : i) *reduced chemistry*, which aims to directly reduced the number of species and reactions from a detailed chemical mechanism, ii) *tabulated chemistry*, where thermochemical quantities of interest are mapped in a low-order manifold and iii) *optimized chemistry* which consist in designing an ad-hoc very small mechanism whose chemical rate constants have been optimized. As shown in Tab. 3, five groups employs reduced schemes whereas the other five use a chemistry tabulation method. All chemical look-up tables are here generated from laminar flamelets: four from premixed 1-D laminar flames [11, 41] and one from a

Team	Institution 1	COLD	MRB18b	MRB26b
Exp	Technische Universität Darmstadt, *Germany* Darmstadt UAS, *Germany* Barlow Combustion Research, *USA*	✓	✓	✓
Num A	EM2C-CNRS, Université Paris-Saclay, *France* Safran Tech, *France*	✓		✓
Num B	Jiangsu University, *China*		✓	✓
Num C	KAUST, *Saudi Arabia* Sapienza University of Rome, *Italia*	✓	✓	✓
Num D	University of Cambridge, *United Kingdom* Peking University, *China*	✓	✓	✓
Num E	Technische Universität Darmstadt, *Germany*			✓
Num F	KTH, Royal Institute of Technology, *Sweden*	✓	✓	✓
Num G	Xi'an Jiaotong University , *China* Beihang University, *China* Eindhoven Univ. of Tech, *Netherlands*	✓	✓	✓
Num H	Université Libre de Bruxelles, *Belgium* BRITE, *Belgium*	✓		✓
Num I	University of Duisburg-Essen, *Germany*		✓	✓
Num J	Universität der Bundeswehr München, *Germany*	✓	✓	

Table 1: Composition of the numerical and experimental teams involved in the joint study. The colored text in the first row indicates the color of the corresponding curves in the radial profile comparisons.

Team	LES solver	Grid (min spacing in mm)	Number of cells	Spatial scheme	Temporal scheme	Turbulent SGS
Num A	YALES2 Low Mach	Structured (0.1)	31 M (same as Num E)	4^{th} order	4^{th} order	Sigma [37]
Num B	OpenFOAM Compressible	Structured (0.02)	4.3 M	2^{nd} order	2^{nd} order	K-equation [39]
Num C	OpenFOAM Compressible	Structured (0.06)	64 M (MRB18b) 8 M (MRB26b)	2^{nd} order	2^{nd} order	WALE [36]
Num D	OpenFOAM Compressible	Structured (0.1)	3.5 M (same as Num H)	2^{nd} order	1^{st} order	Sigma [37]
Num E	OpenFOAM Low Mach	Structured (0.1)	31 M (same as Num A)	2^{nd} order	2^{nd} order	Sigma [37]
Num F	OpenFOAM Low Mach	Hybrid (0.27)	1 M	2^{nd} order	2^{nd} order	WALE [36]
Num G	OpenFOAM Low Mach	Structured (0.15)	3.8 M	2^{nd} order	2^{nd} order	Dyn. Smag. [38]
Num H	OpenFOAM Compressible	Structured (0.1)	3.5 M (same as Num D)	2^{nd} order	2^{nd} order	Smag. [40]
Num I	PsiPhi Low Mach	Structured (0.1)	2.2 B	4^{th} order	3^{rd} order	Sigma [37]
Num J	OpenFOAM Low Mach	Unstructured (0.05)	5.1M	2^{nd} order	2^{nd} order	WALE [36]

Table 2: Numerical strategies followed by the teams. The colored text in the first row indicates the color of the corresponding curves in the radial profile comparisons.

non-premixed counterflow configuration [42, 43]. The difference due to the nature of the chemistry simplification method will not be easily identified in the following result analysis as many other parameter are changing between simulations. This has however been already discussed in the literature, especially within a tabulated chemistry context [9, 44].

3.3. Turbulent combustion modeling

As discussed previously, primary turbulent combustion modeling concepts are also classified in three categories, namely *reactor based*, *statistical* and *geometrical* approaches. As indicated in Tab. 3, the three simulations which model the SGS combustion using Partially Stirred Reactor (PaSR) [24, 51] or Eddy Dissipation Concept (EDC) [46] models fall into the *reactor based* category. *Statistical* approaches are followed by two teams which employ a standard presumed Filtered Density Function (FDF) to close the filtered chemical reaction rate. Interestingly, all groups who prefer a *geometrical* description of the flame front manage the under-resolution with the popular Thickened Flame model for LES (TFLES) [19] also known as the Artificially Thickened flame model (ATF) [27]. A dynamic formulation of the thickening factor is retained with a flame sensor to limit artificial thickening to reacting layers. For all groups choosing such *geometrical* approach, the impact of the turbulence on the flame wrinkling at the SGS scale is captured with the Charlette model [21]. Only one group neglect subgrid scale turbulent effects on the chemistry.

Team	Simp. Chem. model	Turb. Comb. model	Simp. Chem. category	Turb. Comb. category
Num A	Premixed flamelet tabulation [11, 41]	D-TFLES [19, 27] with FWM [21]	TC	Geometrical
Num B	15-species ARC [45]	D-TFLES [19] with FWM [21]	RC	Geometrical
Num C	15-species ARC [47]	EDC [46]	RC	Reactor based
Num D	Premixed flamelet tabulation [11, 41] with transported Y_{CO}[31]	Presumed FDF [48–50]	TC	Statistical
Num E	Premixed flamelet tabulation [11, 41] with transported Y_{CO}[30]	D-TFLES [19, 27] with FWM [21]	TC	Geometrical
Num F	17 species skeletal mechanism [53]	PaSR [24, 51, 52]	RC	Reactor based
Num G	Non-premixed flamelet tabulation [42]	Presumed FDF [54, 55]	TC	Statistical
Num H	15-species ARC mechanism [47]	PaSR [24, 51, 52]	RC	Reactor based
Num I	Premixed flamelet tabulation [11, 41]	D-TFLES [19, 27] with FWM [21]	TC	Geometrical
Num J	19 species ARC [56]	No model	RC	-

Table 3: Chemistry simplification and turbulent combustion models employed by the teams. The colored text in the first row indicates the color of the corresponding curves in the radial profile comparisons. ARC: Analytically Reduced Chemistry; D-TFLES; Dynamical artificial Thickened Flame model for LES, EDC: Eddy Dissipation Concept, FWM: Flame Wrinkling Model, RC: Reduced Chemistry, TC: Tabulated Chemistry.

3.4. Boundary conditions

The numerical teams followed different strategies to define the boundary conditions. The Technical University of Darmstadt performed a cold flow LES of the injector pipes. The solution of this precursor simulation has been used in *Num A*, *Num E* and *Num G* to prescribe the inlet flow velocity of main jet and slot 2, while a laminar parabolic profile has been set for slot 1. Other groups independently defined the boundary conditions, as described in Supplementary Material.

Figure 2 compares all computed mean and RMS axial flow velocity profiles, taken 3 mm above the burner outlet. Black symbols with error bars indicate experimental measurements and uncertainties. Each thin colored solid line represents the solution obtained by one of the nine groups involved in the joint study as indicated in Tab. 1. Most of the simulations correctly recovered the velocity profiles at the burner exit, validating their respective inlet flow velocity parameters. Num B solution however overestimates the mean and RMS velocity profiles at the centerline. As indicated in the Supplementary Materials, the flow upstream the jet inflow is computed in group B simulation. The quality of the mesh in the tube may however not be sufficient to properly compute the turbulent pipe flow. This explains the bias observed in Fig. 6.

All groups prescribed a main jet composition corresponding to equivalence ratio $\phi = 2.6$ ($\phi = 1.8$) in configurations MRB26b (MRB18b), while pure air has been injected trough slot 1. The set-up of slot 2 composition is however controversial because of a slight experimental inconsistency between the flow controllers signal and the Raman species measurements. Indeed, the mixture

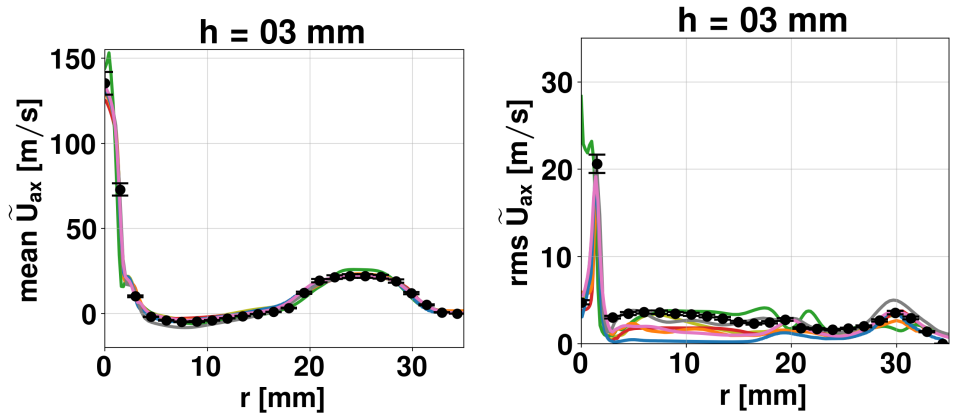

(a) Mean axial velocity

(b) RMS of axial velocity

Figure 2: Mean and RMS radial profiles of the axial flow velocity in the MRB26b case, 3 mm above the burner exit. Black symbols: experiments. Black error bars: measurement uncertainty. Colored solid lines : Solutions from cases given in Tab. 1.

fraction measured at the exit of slot 2 with Raman technique ($Z_{expe} \approx 0.047$) does not exactly correspond to the equivalence ratio of 0.8 ($Z_{\phi=0.8} \approx 0.044$) *a priori* indicated by the flowmeters. This difference generated confusion among numerical teams who adopted different strategies: *Num B*, *Num C* and *Num E* imposed $Z_{slot2} = 0.047$ to fit the species measurements while the other teams set up $Z_{slot2} = 0.044$ as indicated by the flow controllers.

Two LES of the reactive MRB26 cases have been conducted to quantify the sensitivity to Z_{slot2}. Both simulations have been performed with YALES 2 solver on the TUD grid with a premixed flamelet model combined with TFLES (Num A). Only the value of Z_{slot2} is changed between the two simulations.

Computed mean radial profiles of the mixture fraction are compared

against experimental data for both cases ($Z_{slot2} = 0.047$ and $Z_{slot2} = 0.044$) in the expanded view shown Fig. 3 (a). Radial profiles of mixture fraction taken 6 mm above the burner exit show that, as expected, with $Z_{slot2} = 0.044$, the mixture fraction radial profiles underpredict the Raman measurements taken above slot 2 exit (20 mm $<$ r $<$ 30 mm). This is corrected by $Z_{slot2} = 0.047$ simulation. Interestingly, the mixture fraction in the recirculation zone (4 mm $<$ r $<$ 20 mm) becomes to be impacted by the change of slot 2 composition only from $h = 30$ mm. For $h = 6$ mm and $h = 15$mm, the recirculating burnt gases mixture fraction remains slightly under estimated by the simulation.

Fig. 3 (b) shows a minor effect on the temperature profiles. Only the expanded view shown in Fig. 3 (c) reveals a bias of approximately 50K within the burnt gases recirculation zone from h=30 mm. This is retrieved through adiabatic thermo-chemical equilibrium computations which indicate that the differences in element composition induced by ΔZ_{slot2} cause a similar bias of burnt gas temperature. Finally Fig. 3 (d) show a minor impact of slot 2 composition on the CO mass fraction, where only the peak in the outer flame is affected. The impact of Z_{slot2} uncertainties remains then moderate.

Adiabatic conditions have been assumed at the wall boundaries by all groups. This assumption has been justified by complementary TUD simulations, which showed that accounting for heat losses at the burner lip separating the main jet from slot 1 does not significantly affect the turbulent structure of the flame [57].

Further information are give in the Supplementary Materials, where the numerical and modeling set-up are detailed group by group.

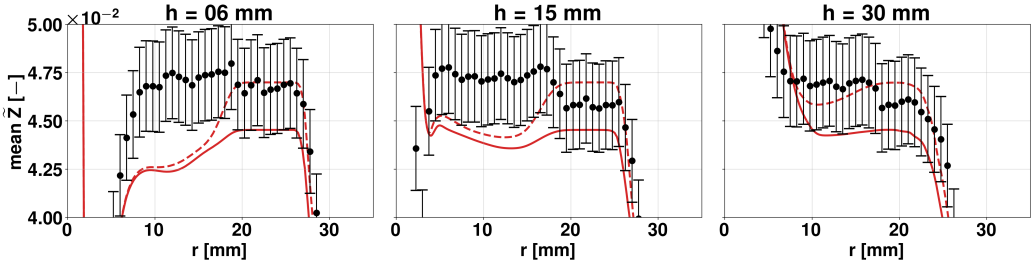

(a) Mean mixture fraction (expanded view)

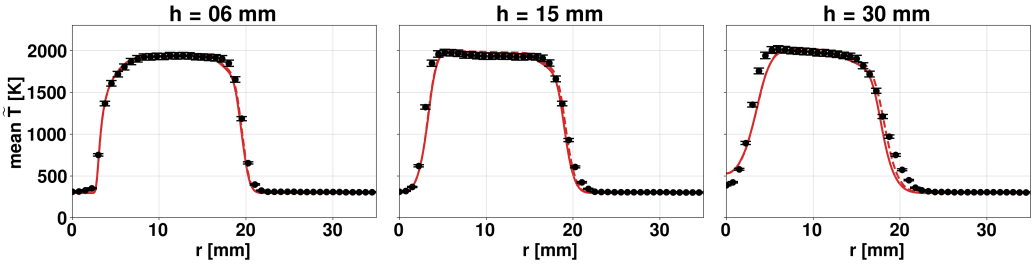

(b) Mean temperature

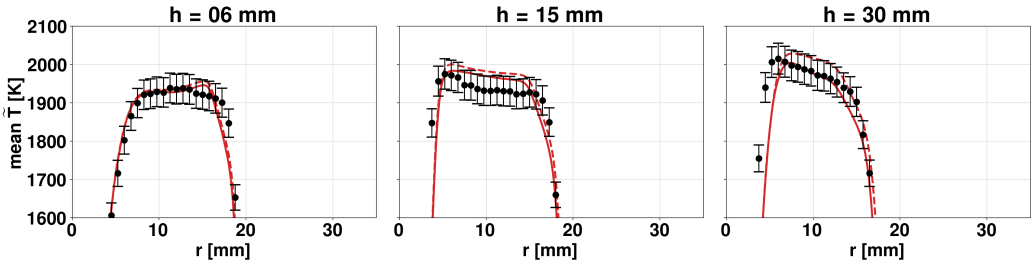

(c) Mean temperature (expanded view)

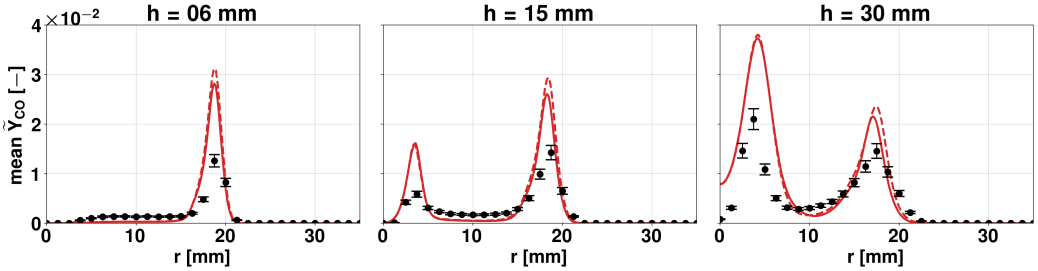

(d) Mean CO mass fraction

Figure 3: Sensitivity analysis of the fresh gas composition injected through slot 2 on the mean radial profiles. Black symbols: experiments. Black error bars: measurement uncertainty. Solid lines : numerical solutions with $Z_{slot2} = 0.04454$. Dashed lines: numerical solutions with $Z_{slot2} = 0.047$.

4. Results

4.1. Cold flow simulations

As indicated in Tab.1, eight groups perform the cold flow simulation. Comparisons between experimental data and numerical results are presented in the supplementary materials. Despite the significant variation in the numerical scheme, grid quality, and turbulent SGS closures between simulations, a good agreement is reached between the simulations and the measurements. This observation suggests that the differences later observed in the reactive cases will mainly be due to the flame computing (including combustion modeling and numerical resolution of the reactive laver).

4.2. Flame topology and lift-off

Instantaneous snapshots of 2-D temperature iso-contour are shown in Fig. 4 for a selection of 8 computations, ordered by grid size from left to right and top to bottom. The same grey scale has been adopted ranging from 300K (black color) to 2300K (white color). All simulations predict the recirculation zone, filled with hot burnt gases, which is formed behind the bluff-body. The influence of the mesh resolution on the turbulent flame structure is clearly evidenced; while the flame computed on the very coarse grid is almost not perturbed by the flow, the highly resolved flames exhibit a very fine level of resolved flame wrinkling. Differences are evidenced on the jet penetration whose length seems sensitive to the grid resolution. Figure 5 shows 2-D views of the progress variable reaction rate, where black and white color correspond to 0 and peak value, respectively. A quantitative comparison of the images is not possible, as each group used different progress variable

definitions. It is however observed that all simulations retrieve the two main reaction zones identified in the experiments [29]:

- An outer reaction zone is stabilized by the burnt products recirculating behind the bluff-body and consumes reactant from slot 2. As the fresh equivalence ratio is within the flammability range of methane-air, the combustion regime is dominantly premixed here.

- An inner lifted flame downstream of the jet and slot 1 is supported by hot products and exposed to high stratifications. The GRFI analysis conducted [29] showed that this reaction zone exhibits a very complex turbulent flame dominated by multi-regime structures interacting with both premixed and non-premixed local flame zones.

The recent analysis performed from flow field and flame front tracking measurements [32] explained the stabilization mechanism. A mixture within flammability limits is first generated in the shear layer located between slot 1 and the central fuel jet. In the meantime, the recirculation zone behind the bluff body, filled with burnt gases produced by the outer lean flame, entrains hot products toward this flammable mixture. The combined increase of flame speed due to the high turbulence levels and elevated temperature in the shear layer then allow a lifted flame to stabilize above the jet and slot 1. Instantaneous 2D views of the progress variable reaction rate show that all simulations predicted well a lifted flame structure. Most of the numerical solutions quite well agree on the position of the inner flame front tip (indicated by the horizontal red solid line). Only *Num F* predicts a very low lift-off height, which can be attributed to a poor grid resolution.

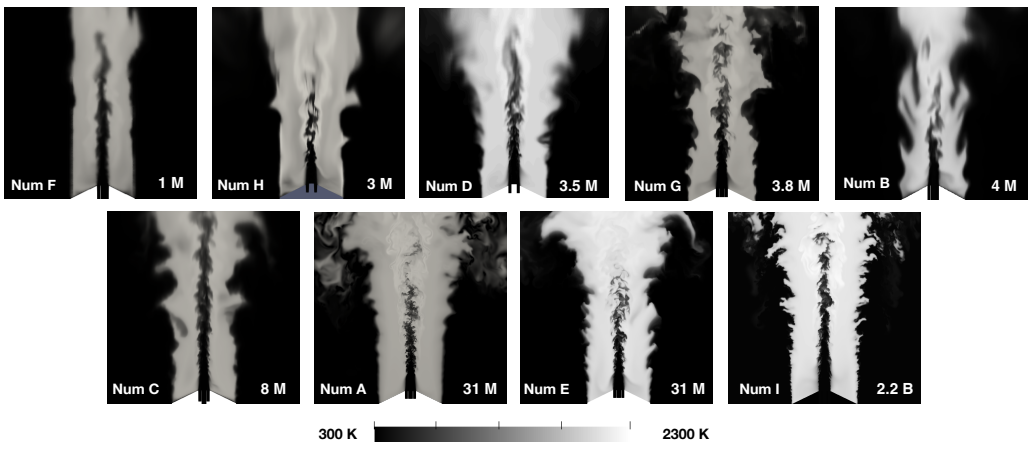

Figure 4: 2D iso-contour of temperature extracted from nine simulations of MRB26b case. Increasing mesh size from left to right and top to bottom. Numerical team and number of grid elements are indicated on the bottom left and right corners of each figure, respectively.

4.3. Radial profiles

Similar observations have been made when analyzing numerical data from MRB18b and MRB26b, therefore only computational results from MRB26b are discussed in the following sections. Mean radial profiles from MRB18b are available in Supplementary Materials.

Mean and RMS of the axial and radial components of the velocity field are shown in Fig. 6 for the case MRB26b. Results are plotted over the radius direction at four axial positions: h = 6, 15, 30 and 60 mm. The colors corresponding to each simulation are indicated in Tab. 1 and reminded in the color key embedded in the top of the figure. As many parameters are changing between the simulations (grid, numerical methods, BC's, subgrid closures models, etc.), a curve-by-curve analysis is of little interest, that is why the color key will not be repeated in the following figures. However,

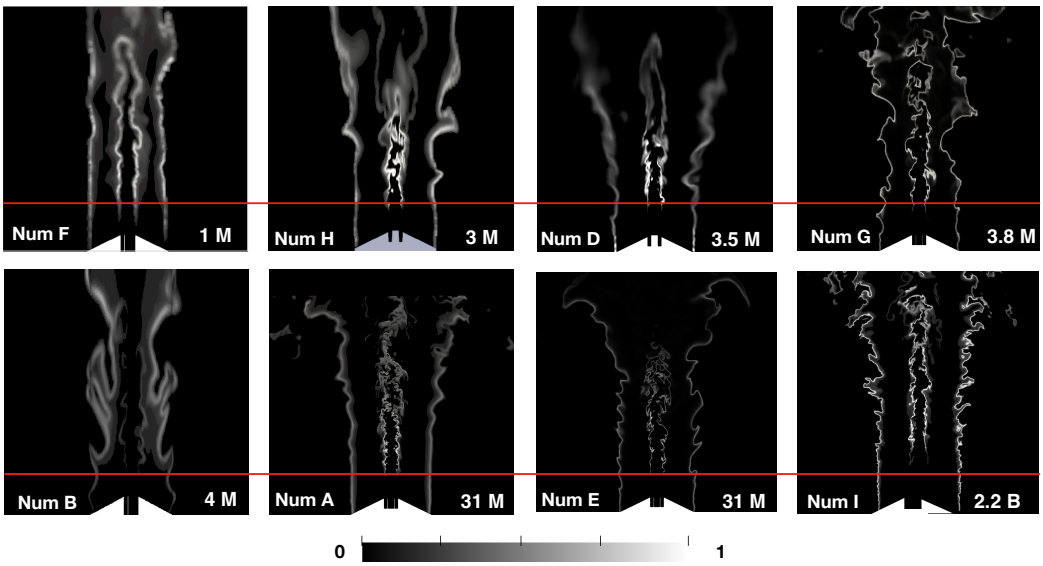

Figure 5: 2D iso-contour of normalized progress variable reaction rate extracted from eight simulations of MRB26b case, with increasing mesh size from left to right and top to bottom. The reaction rate was normalized so that the maximum value corresponds to 1. Numerical team and number of grid elements are indicated on the bottom left and right corners of each figure, respectively. The solid red horizontal line is positioned arbitrarily at a given axial position to facilitate visual comparison of flame lift off heights. The source term has been divided by the thickening factor for TFLES simulations (Num A, Num E and Num I)

since we are fortunate to have ten numerical solutions, a rough statistical analysis is possible. The red symbols are then the average of the nine individual solutions while the red vertical error bars indicate the amplitude of the standard deviation of the simulations. Mean and RMS of axial velocity are remarkably well predicted by all groups while radial velocity fields remains satisfactorily captured, although an overestimation is observed downstream, in the outer flame region. Significant discrepancies are however observed

between Num B and other group solutions. This bias is attributed to the misprediction of the inflow boundary condition discussed previously. The error propagates downstream and affect the quality of the shear layer prediction). As expected, simulations performed on the finest grid (Num I) leads to an excellent prediction of the flow field.

Despite such discrepancies, these results illustrate the general ability of LES flow solvers to capture the flow dynamical of jet flames, as observed in the previous TNF joint study [28].

Mean and RMS radial profiles of the mixture fraction, plotted in Fig. 7, are well predicted by the simulations. In particular, simulations conducted on the finest mesh (Num I) present the best agreement. However, the expanded view (Fig. 7c) shown behind the bluff-body, in the flow recirculating between slot 1 and slot 2, reveals significant disagreements in the element composition. The reason is the differences in the composition of the mixture injected through the slot 2, as discussed previously in Sec. 3.4.

Figure 8 shows the mean and RMS radial profiles of temperature fields. The inner flame front position (3 mm $<$ r$<$ 8 mm) is well computed at the first three axial positions: h = 6, 15 and 30 mm. Indeed, the average of the computations matches the experimental measurements while the numerical variance remains comparable with the experimental uncertainty. The outer flame (17 mm $<$ r $<$ 22 mm) is also fairly captured even if the simulations present a larger dispersion.

Discrepancies are more pronounced downstream, at h = 60 mm. In addition to disagreeing on average with the experiments, simulations exhibit a very large scatter. Note that the misprediction of the outer flame front po-

(a) Color legend

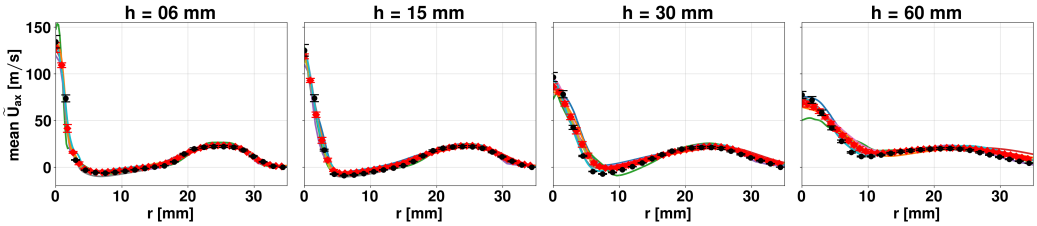

(b) Mean axial velocity

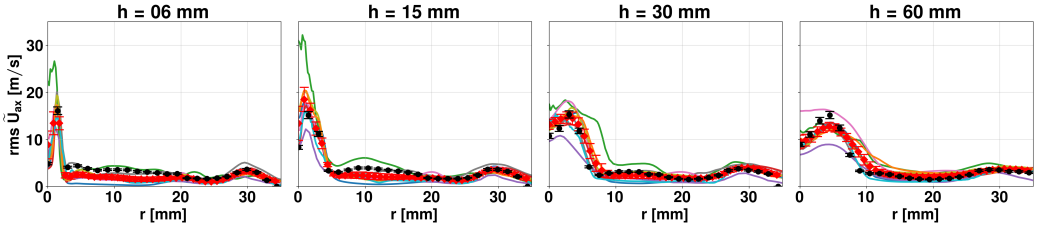

(c) RMS of axial velocity

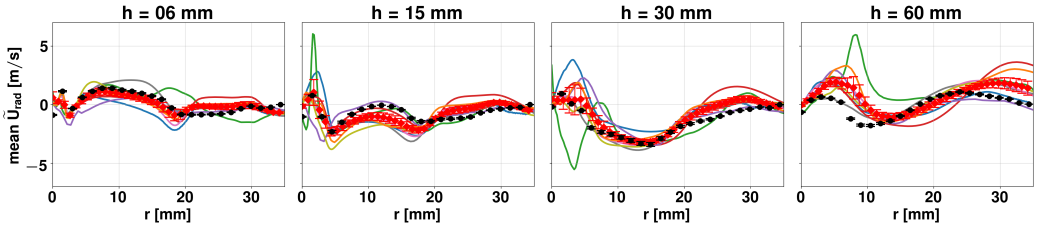

(d) Mean radial velocity

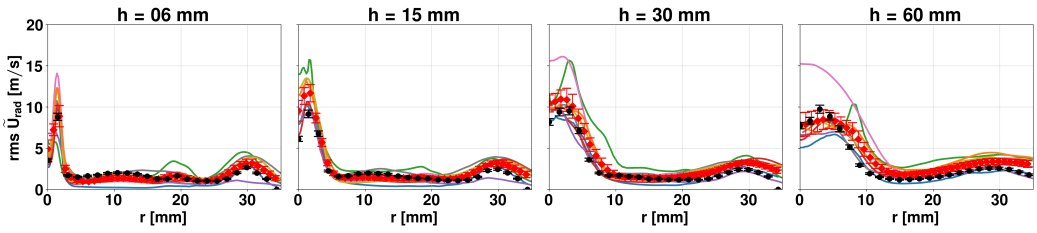

(e) RMS of radial velocity

Figure 6: Flow velocity in the MRB26b case. Black symbols: experiments. Black error bars: measurement uncertainty. Colored solid lines : Solutions from cases given in Tab. 1. Red symbols: average of all numerical solutions. Red vertical error bars: amplitude of the standard deviation of the simulations.

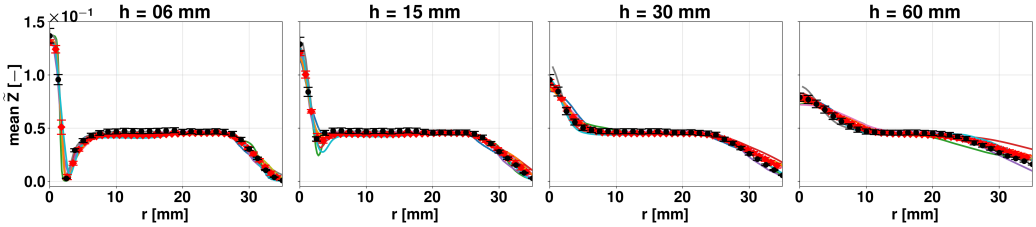

(a) Mean mixture fraction

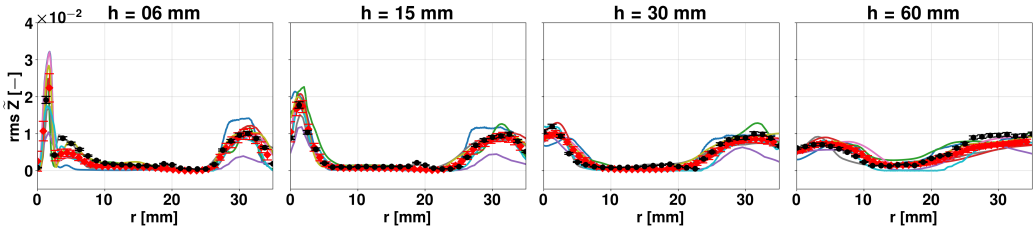

(b) RMS of mixture fraction

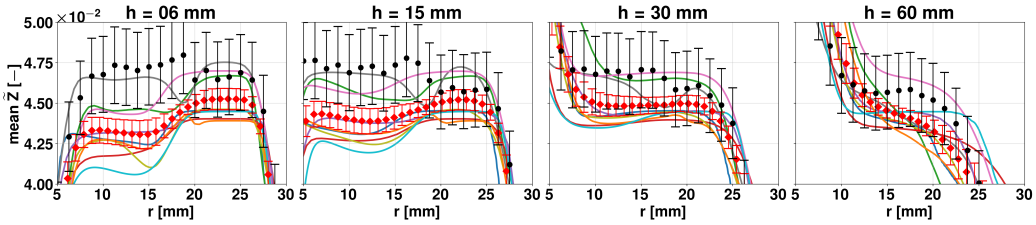

(c) Mean mixture fraction (zoom in the recirculation zone)

Figure 7: Mixture fraction in the MRB26b case. Black symbols: experiments. Black symbols: experiments. Black error bars: measurement uncertainty. Colored solid lines : Solutions from cases given in Tab. 1. Red symbols: average of all numerical solutions. Red vertical error bars: amplitude of the standard deviation of the simulations.

sition is correlated to the computing errors of the radial velocity previously observed in Fig. 6. The finely resolved grid (Num I) performs less in terms of temperature than the flow and mixing fields. This is assumed to be a consequence of lack of heat transfer modeling in the burner cap and the use of less accurate chemistry and turbulent combustion models.

Fig. 6(c) shows that, in the outer flame region, resolved RMS of temperature are bellow the measured data. As the plotted LES RMS does not include the subgrid scale RMS, conclusions regarding the simulation performances in terms of flame turbulence interactions are difficult. However, it is observed that LES RMS remains lower than measured RMS, as expected from theory.

The expanded view in the bluff-body region shown in Fig. 8 (bottom) presents a deviation of the computed temperature from the measurements in the recirculation zone which can reach 250K. A first possible explanation is the under-prediction of the mixture fraction, highlighted in Fig. 7 (c). This might be due to some additional air entrainment from slot 1 or by the unity Le assumption, which leads to the under-prediction of the species accumulation in the recirculation zone as pointed out in [58–60]. Other possible source of error are the chemistry reduction method or the turbulent combustion model closures assumptions. Finally heat losses at the burner lips may also have a small impact. Complementary discussions on the difficulty to simulate the temperature field in the MRB configuration are available in [61].

Mean and RMS radial profiles of CO mass fraction are shown in Fig. 9. CO is present in the outer flame front (17 mm $<$ r $<$ 22 mm) starting from the burner exit, but starts to be produced in the inner reactive layer (3 mm $<$ r $<$ 8 mm) farther downstream from h = 15 mm. While computed mean

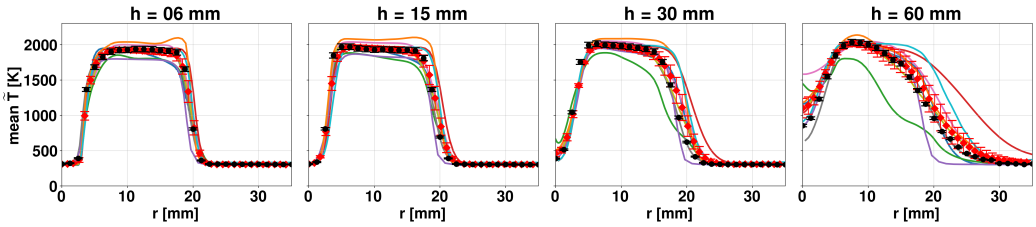

(a) Mean temperature

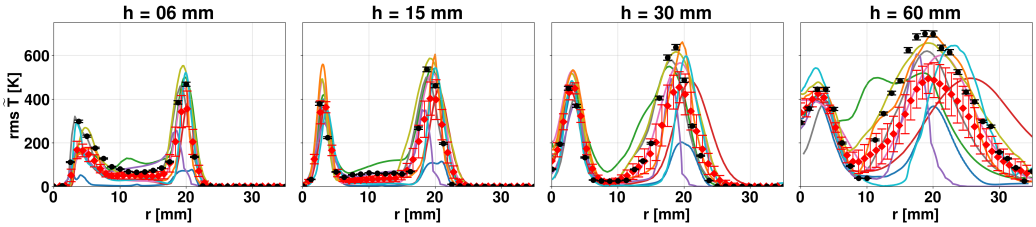

(b) RMS of temperature

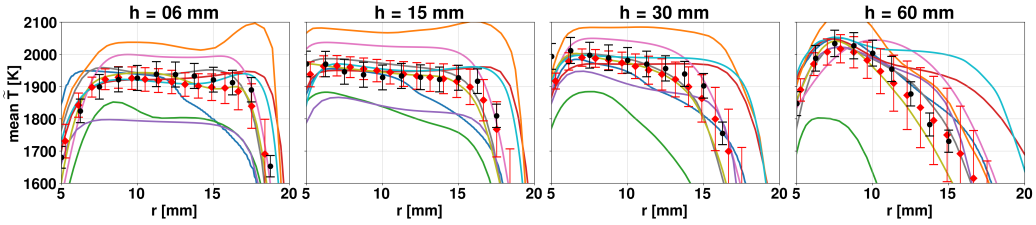

(c) Mean temperature (zoom in the recirculation zone)

Figure 8: Temperature in the MRB26b case. Black symbols: experiments. Black error bars: measurement uncertainty. Colored solid lines : Solutions from cases given in Tab. 1. Red symbols: average of all numerical solutions. Red vertical error bars: amplitude of the standard deviation of the simulations.

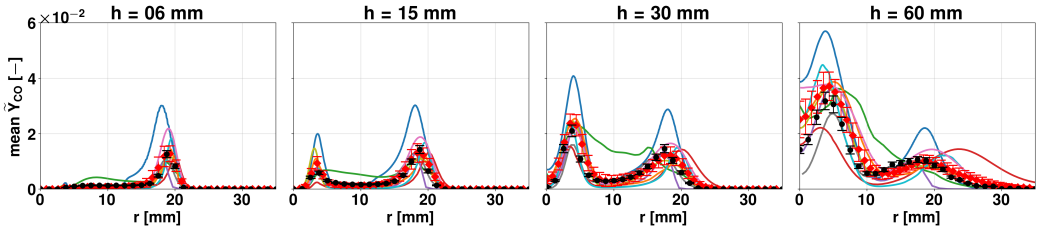

(a) Mean CO mass fraction

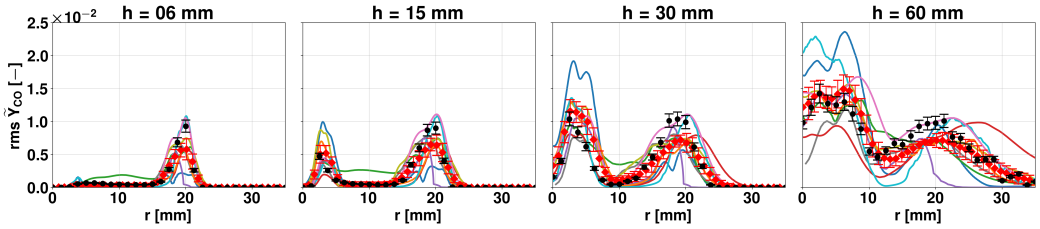

(b) RMS of CO

Figure 9: CO mass fraction in the MRB26b case. Black symbols: experiments. Black error bars: measurement uncertainty. Colored solid lines : Solutions from cases given in Tab. 1. Red symbols: average of all numerical solutions. Red vertical error bars: amplitude of the standard deviation of the simulations.

CO profiles are close to experimental data, the dispersion of the simulation data is very high: the numerical uncertainty of the computed peak of CO mass fraction is about 30-40 % for both inner and outer flame fronts. The reason of these differences are discussed first in the outer flame front and then in the inner flame front.

4.4. Outer flame analysis: on the impact of artificial flame thickening on the CO mass fraction

The analysis first focuses on the outer flame reactive layer, characterized by a standard turbulent premixed regime. Figure 10 sorts the numerical so-

lution by simplified chemistry methods. Most of the four reduced chemistry solutions (orange solid lines) give satisfactory estimates of the peak of CO, especially at the first three axial positions. Surprisingly, the premixed-based tabulated chemistry approaches (blue solid lines) significantly over-predict the carbon monoxide production. This results is not consistent with previous analysis [14, 44] which concluded that FPI or FGM should capture accurately the chemical structure of premixed flame reaction zone. To understand the reason of this deviation, results are now sorted by turbulent combustion models in Figure 11. While statistical and reactor based results are distributed around the experimental data, the three solutions issued from the geometrical approach (blue solid lines) significantly over predict the experimental measurement of CO mass fraction. For these three computations, the flame front under-resolution has been managed with an artificial thickening of the flame front. This mathematical operation retrieves the correct flame consumption speed but does not conserve the species mass as discussed in [62]. Recent LES of turbulent premixed flames observed that it may cause significant over-predictions of intermediates species peak values, such as the CO, in the flame brush [63, 64].

An illustration of this effect is obtained by manufacturing a mean, pseudo 1-D, flame brush from a large number of laminar flamelets, following the idea suggested by Vervisch et al. [65]. A synthetic turbulent flame is manufactured by a random distribution of 5 000 detailed chemistry premixed laminar flamelet solutions. All solutions are identical (same thickness and chemical structure) but are localised at different positions. This procedure mimics a 1-D DNS performed in the flamelet regime as flamelet profiles are transported

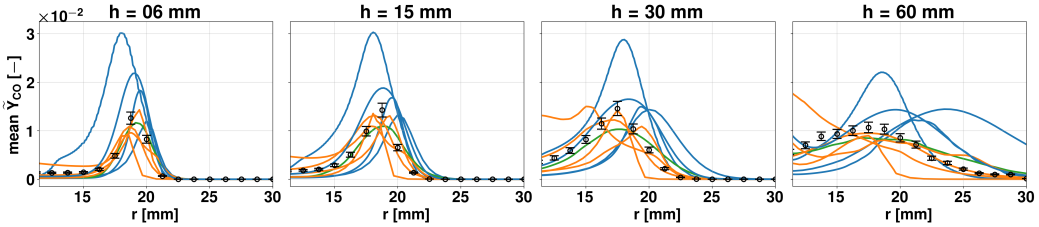

Figure 10: Mean radial profiles of CO mass fraction in the MRB26b case sorted by the type of simplified chemistry model. Zoom in the outer flame region. Symbols: experimental data. Blue solid lines: premixed based tabulated chemistry. Green solid lines: non-premixed based tabulated chemistry. Orange solid lines: reduced chemistry.

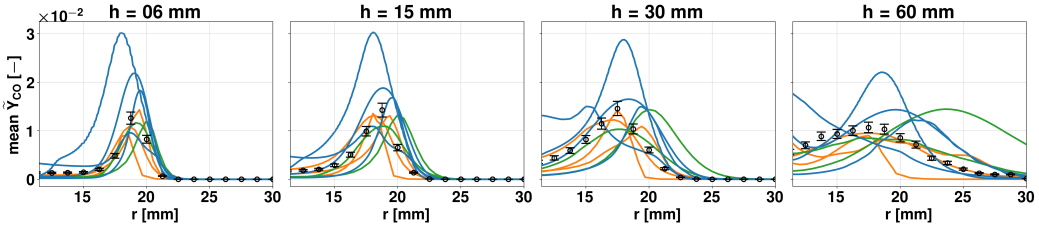

Figure 11: Mean radial profiles of CO mass fraction in the MRB26b case sorted by the type of turbulent combustion model. Zoom in the outer flame region. Symbols: experimental data. Blue solid lines: geometrical. Green solid lines: statistical. Orange solid lines: reactor based.

by turbulence without modification of their internal structure.

Figure 12(a) shows an example of premixed flamelet distribution whose statistical properties have been adjusted to match the flame brush thickness, measured in the outer flame reaction zone at h=6 mm and defined here as $\delta_{\widetilde{T}} = (\widetilde{T}^{BG}_{Exp} - \widetilde{T}^{FG}_{Exp})/(\max(d\widetilde{T}/dx)$, where superscripts FG and BG denotes fresh and burnt gases conditions, respectively. Averaging this ensemble of planar flame solutions provides a mean CO profile shown by the bold black

solid line, which only accounts for the intermittency property of the flame brush.

Assuming flamelet regime, the 3-D wrinkling patterns tends to increase the averaged mass of CO. This phenomena, extensively discussed in [66], has been observed both by post-processing 3-D DNS of the Preccinsta burner solution [67] and by filtering filtered-wrinkled manufactured flamelets. The lower limit of CO production is therefore given by the average of planar (not wrinkled) 1-D premixed flames, illustrated by the bold black solid line in Fig 12(a). The impact of multi dimensional wrinkled flame patterns induced by turbulent motions is difficult to quantify *a priori* as it depends of the subgrid flame wrinkling modeling [66]. However, if we neglect the influence of strain rate of the chemical flame structure, the maximum peak of CO is simply given by an instantaneous planar unstretched flame solution. The measured peak of CO is then located between an "steady laminar" upper limit given by steady laminar flame solution (which does not consider intermittency) and "laminar intermittent" limit provided by the manufactured mean profile. It means that an LES simulation, which assumes the flamelet regime, will provide a solution between these two limits. An accurate computation of the resolved flame wrinkling combined with an efficient sub-grid scale flame wrinkling model may then hopefully provide the right answer.

The same procedure is now applied on a random distribution of thickened flame solutions. Results are plotted in Fig. 12(b) for a thickening factor of 4. While the upper limit is not affected by the artificial thickening, the lower limit is significantly increased, even exceeding the experimental data. An LES computation based on such thickened flame archetype would therefore

never capture the chemical turbulent flame structure, no matter how accurate is the flame wrinkling resolution and modeling as the CO mass fraction would be systematically overestimated.

Figure 13 shows, at three streamwise positions (h=6, 15 and 30 mm), a comparison between the actual LES solution computed with TFLES model and the corresponding mean manufactured thickened flame solution. Three thickening factor are considered: F=1.5, 4 and 8.5, corresponding to *Num I*, *Num D* and *Num A*, respectively. As expected, peak values of all LES solutions, obtained with a thickening factor F, lie between their corresponding lower boundary given by averaging laminar flamelets, also thickened with the same factor F, and the "steady laminar" boundary (given here by Y_{CO}=0.032). For large thickening factors (F=4 and F=8.5), "laminar intermittent" limit exceed the experimental data at the three axial location. Under theses conditions, the LES will inevitably overpredict the CO production. The comparison also shows that for higher flame thickening factors, the TLES solutions are closer to the manufactured "intermittent laminar " flame brush limit. It means that the resolved 3-D flame wrinkling patterns are not significant anymore and the flame front is almost laminar. The reason is the lower sensitivity of the thickened flame to the resolved turbulent motion [68]. Logically, results obtained on the finest grid (Num I) present the best agreement against experimental data, since the flame is the least thickened.

Finally, it is worth noting that the non-premixed-based tabulation (green solid line in Fig. 10) yields better prediction than the premixed-based tabulation for Y_{CO} prediction in the outer flame region. This counter intuitive result is explained by two reasons. First, the non-premixed flame tabula-

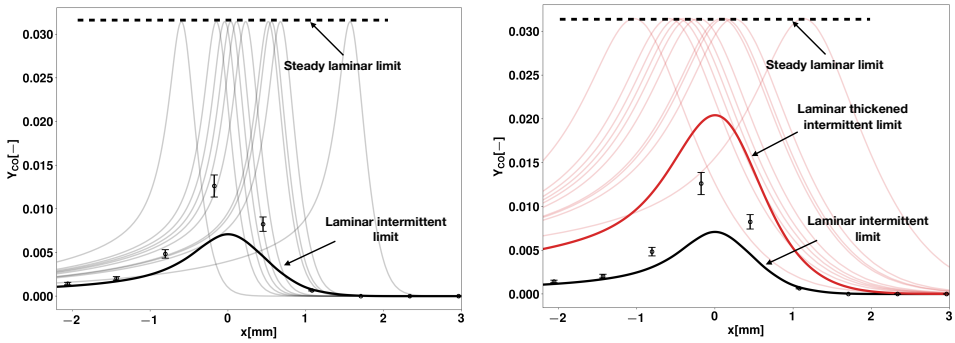

Figure 12: Manufactured pseudo 1-D turbulent flame brush whose thickness matches the one measured 6 mm downstream the burner exit. Thin lines show a sample of the randomly distributed flamelet solutions. Bold lines are the Reynolds averaged mean profiles. Symbols are the experimental data measured at h=6 mm. Left: without artificial flame thickening (F=1). Right: with artificial flame thickening (F=4).

tion adopted by Group G [42, 43] includes both of the steady and unsteady straining flamelets. The method captures the whole process of the flamelet straining and extinction, and results in a chemical database that is very similar to the premixed flame tabulation, especially when the straining rate is relatively low. Second this method does not employ artificial flame thickening, which biases the CO prediction as discussed previously.

4.5. Inner flame analysis: on the ability to capture multi-regime combustion

The analysis focuses now on the inner flame region (3 mm $<$ r $<$ 8 mm), where multi-regime combustion patterns are dominant [29]. Numerical solutions are again sorted by simplified chemistry assumption and turbulent combustion model approaches, in Figs. 14 and 15, respectively. As in the

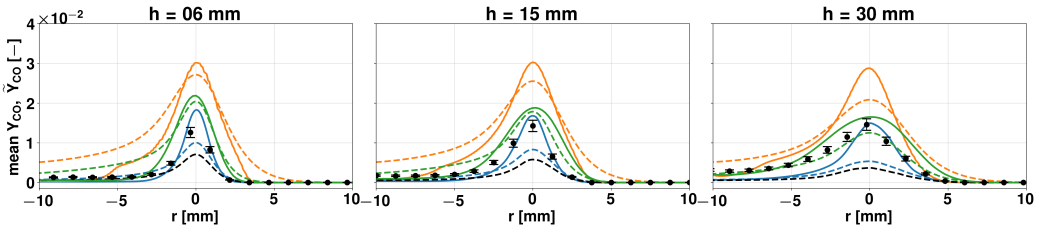

Figure 13: Comparison between LES solutions computed with TFLES model and the corresponding mean manufactured thickened flame solutions. Solid lines: LES solutions. Dashed lines: manufactured solutions. Symbols: experimental data. Black: F=1 (no-thickening). Blue: F=1.5 (*Num I*). Green: F=4 (*Num D*). Orange: F=8.5 (*Num A*).

outer flame, the numerical solutions show a large dispersion around experimental data without any approach standing out from the others. Regarding the impact of simplified chemistry assumptions shown in Fig. 10, an expected source of modeling error is the inaccuracy of the premixed-flamelet manifold to capture multi-regime flame structure. However, this impact appears to be negligible compared to the bias induced by the artificial thickening of the flame, highlighted by the solid blue lines in Fig. 11, which is very similar to that observed in the analysis of the outer flame. Because of the multiple source of errors, it is difficult to draw a consolidated explanation of the simulations differences. However, we can note that despite the greater complexity of the inner flame structure, the results are not worse than the outer flame simulation.

4.6. Scatter plot analysis

The discussion now focuses on the ability of the approaches to qualitatively track chemical trajectories disregarding errors in flow prediction. For this purpose, scatter plots of temperature are first shown in Fig. 16 for the

three axial positions h = 6, 15 and 60 mm. Data taken at the position h = 6 mm are located below the base of the lifted flame. Inert mixing between jet and air from slot 1 and between slot 1 and the outer flame products correspond to lines a and b shown in the experimental scatter plot. The vertical line c illustrates the premixed flame brush fed by slot 1 fresh gases. All simulations agree and capture these phenomena.

At h = 15 mm, reactions begin to occur in the inner flame region. The area covered by blue scatter plot illustrates reaction of samples located in the inner flame region. As discussed in [29], this region is characterized by the lines b_l and b_r, which correspond to the lean and rich boundaries, respectively. While all simulations capture the shape of the area covered by inner flame trajectories, significant differences are highlighted in the position of b_l and b_r. Moving farther downstream, the range of mixture fraction decrease, and numerical trajectories mainly agree with the experimental reference.

Scatter plots of CO mass fractions are shown in Fig. 17. While the production of CO is fairly captured above the burner exit (h=6 mm) differences progressively increase when moving downstream. Significant differences are highlighted in both the amount of CO produced and the accessed trajectories, especially at h=60 mm.

The Wasserstein metric [69, 70] is now introduced to quantitatively compare the experimental and numerical scatter data. This post-processing tool, defined as the weighted average of the pair-wise distances between samples of numerical (N) and experimental (E) distributions is well adapted to analyse combustion LES results [71, 72]. Each element of the empirical distributions n_i and e_j contains information for three considered scalars: the mixture frac-

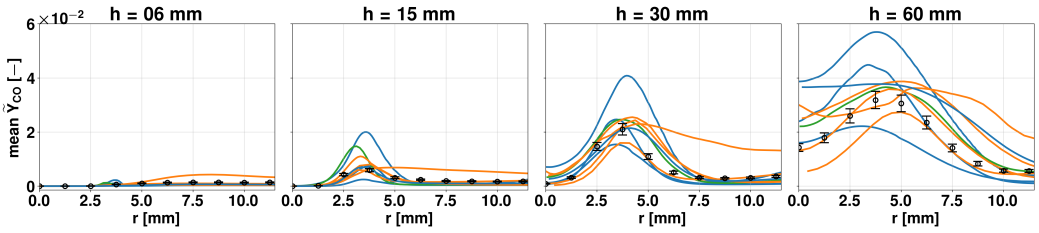

Figure 14: Mean radial profiles of CO mass fraction in the MRB26b case sorted by the type of simplified chemistry model. Zoom in the inner flame region. Symbols: experimental data. Blue solid lines: premixed based tabulated chemistry. Green solid lines: non-premixed based tabulated chemistry. Orange solid lines: reduced chemistry.

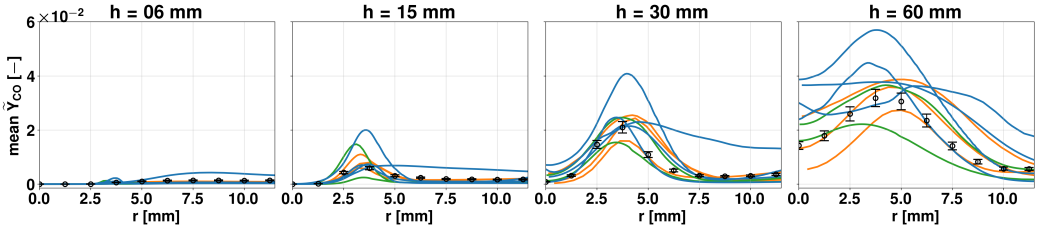

Figure 15: Mean radial profiles of CO mass fraction in the MRB26b case sorted by the type of turbulent combustion model. Zoom in the inner flame region. Symbols: experimental data. Blue solid lines: geometrical. Green solid lines: statistical. Orange solid lines: reactor based.

tion Z, the temperature T and the CO mass fraction Y_{CO}. The 2^{nd} Wasserstein metric is computed as solution of the following minimization problem:

$$W_2(Z,T,Y_{CO}) = \min_{\Gamma} \left(\sum_{i=1}^{n} \sum_{j=1}^{n'} \gamma_{ij} c_{ij} \right)^{1/2} \tag{1}$$

where Γ is the optimal transport matrix having elements γ_{ij} and dimension $n \times n'$. The unit transportation cost c_{ij} is defined as the 2^{nd} power of the

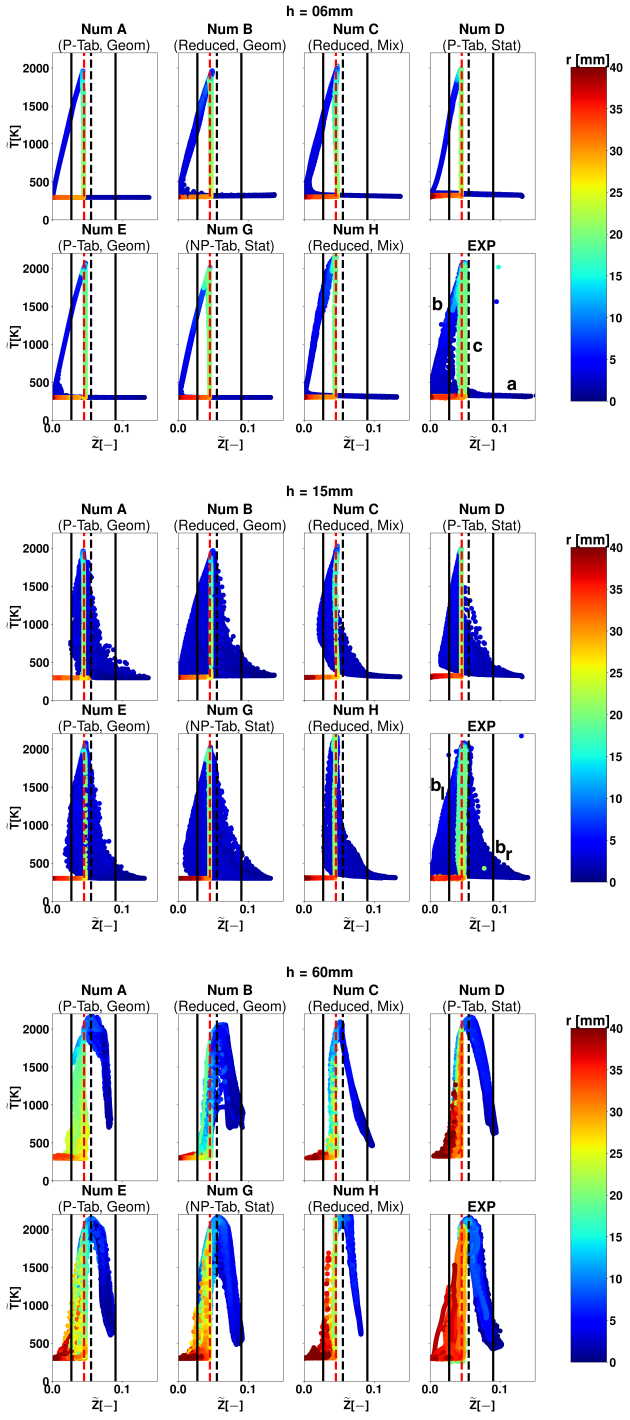

Figure 16: Instantaneous scatter data for temperature versus mixture fraction Z at three axial locations.The vertical dashed line (black) in each plot marks the stoichiometric mixture fraction. The vertical solid lines (black) indicate the flammability limits and the vertical dashed line (red) correspond to slot 2 conditions.

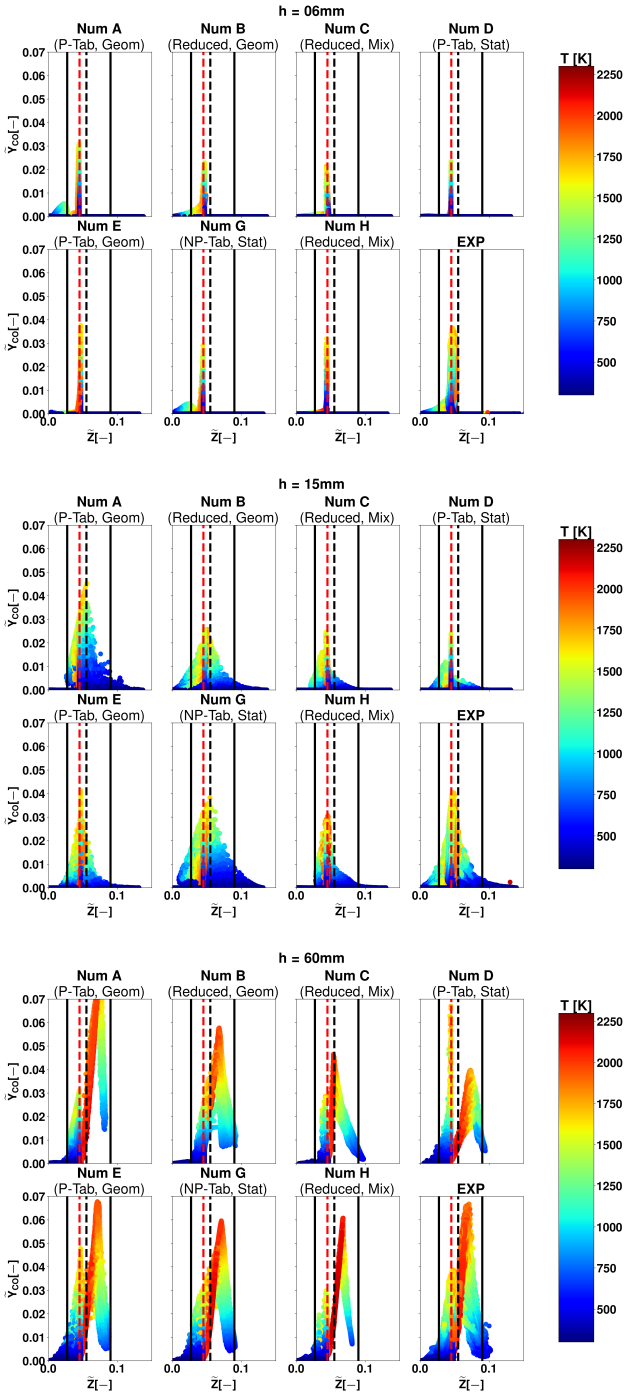

Figure 17: Instantaneous scatter data for temperature versus mixture fraction Z at three axial locations.The vertical dashed line (black) in each plot marks the stoichiometric mixture fraction. The vertical solid lines (black) indicate the flammability limits and the vertical dashed line (red) correspond to slot 2 conditions.

pair-wise Euclidean distance: $c_{ij} = \sum_{v=1}^{N_v}(n_{v,i} - e_{v,j})^2$, where v, is the vth of variable investigated, and $N_v = 3$ is the total number of scalar quantities. The Wasserstein metric is here applied to the MRB configuration at three axial locations corresponding to h=6 , 15 and 60 mm by using the code provided in [71]. Experimental and numerical scatter data are downsampled by selecting 1000 points. Figures 18 and 19 shows the cumulative Wasserstein metric for all numerical solutions, normalized by the standard deviation of the experimental distribution. As in [71, 72], the metric is decomposed in the single variable contributions to identify the source of error. The Wasserstein metrics are first sorted by type of chemistry model in Fig. 18. The cumulative and normalized metric $W_2(Z, T, Y_{CO})$ shows that tabulated chemistry performs as well as reduced chemistry, although it is *a priori* less accurate in multi-regime combustion. However the analysis by turbulent combustion model shown in Fig. 19 presents larger discrepancies in the geometrical approaches solutions, especially for temperature and CO. This observation is consistent to the bias induced by the artificial flame front thickening previously discussed in 4.4.

4.7. Computational costs

Computational details are provided in table 4 . The reported data do not accurately compare code performance since different MPI implementations, compilers, interconnects, and CPU-cores were used. It highlights, however, the very large variation of the computational resources involved. The number of cores used by the groups varies by more than two orders of magnitude (from 108 to 65 536 cores). Also, the differences between the cheapest and most expensive calculation are three orders of magnitude (from 9.7×10^3

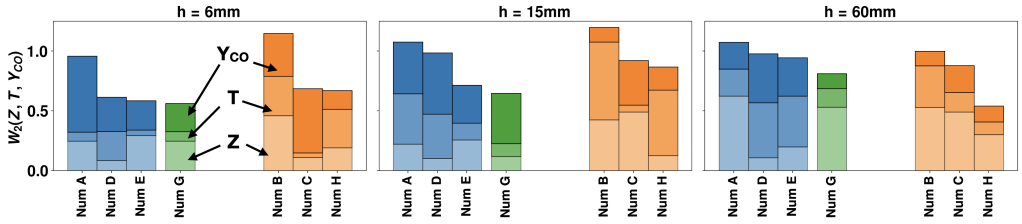

Figure 18: Normalized cumulative multi-scalar 2^{nd} Wasserstein metric for three different axial locations: h=6 , 15 and 60 mm. Simulations are sorted according to the chemistry modeling. Blue : premixed based tabulated chemistry. Green : non-premixed based tabulated chemistry. Orange: reduced chemistry. For each simulation results, the metric is decomposed in the three single variable contributions : mixture fraction, temperature and CO mass fraction (from bottom to top).

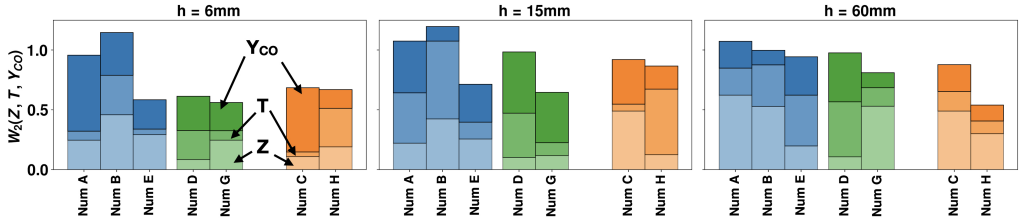

Figure 19: Normalized cumulative multi-scalar 2^{nd} Wasserstein metric for four different axial locations: h=6 , 15, 30 and 60 mm. Simulations are sorted according to the turbulent combustion modeling. Blue : geometrical. Green : statistical. Orange: reactor-based. For each simulation results, the metric is decomposed in the three single variable contributions, from bottom to top: mixture fraction, temperature and CO mass fraction.

to 7000×10^3 CPU hours). A measure of the computational cost (CC), independent of the grid size, is introduced as :

$$CC = \frac{T}{t \times n} \tag{2}$$

where T, t, and n are the core time, the physical time, and the number of cells.

Being the only code to take advantage of structured connectivity, the PsiPhi code is much more efficient than OpenFoam and Yales 2 ($CC = 28$). The cost of simulations C and D is also affected by the use of a compressible code that limits the time step to the acoustic scale. The differences between the other groups may be explained by the different categories of the turbulent combustion model. The efficiencies reached by simulations A, B, and E, which are based on a geometrical description of the turbulent flame propagation, are comparable ($CC = 202; 343; 353$). Simulations D and G, which used a presumed PDF formalism, presents a similar CPU cost ($CC = 226; 524$). Simulations obtained with the reactor-based approaches (groups C, F and H) are slightly more expensive as they requires the local resolution of a detailed chemistry reactor model on each grid cell ($CC = 648; 666; 682$).

5. Conclusions

This joint numerical study of the MRB burner aims to partially illustrate the ability of the turbulent combustion modeling community in terms of multi-regime flame simulations. For that purpose, ten numerical groups and one experimental team collaborate within the framework of the TNF workshop. Simulations were performed on three different LES solvers: OpenFOAM (8 groups), YALES2 (1 group), and PsiPhi (1 group). Chemistry was

simplified by using premixed flamelet tabulation (4 groups), non-premixed flamelet tabulation (1 group), and reduced chemical schemes (5 groups). The turbulent combustion models employed, representative of the three main modeling strategies, are the geometrical (4 groups), statistical (2 groups) and reactor based (3 groups) approaches. One team did account for subgrid scale fluctuation of chemical reaction rates. Different grid resolutions were employed with mesh sizes ranging between 1 million and 2.2 billion cells.

The comparison of 2-D instantaneous snapshots of heat release along the centerline planes evidenced a high sensitivity of the lift-off height prediction to the mesh resolution. Increasing the mesh resolution improves the prediction of mixing phenomena and therefore the location of the region where chemical reactions are initiated.

Detailed comparisons between experimental and numerical data along radial profiles taken at different axial positions showed that the temperature field is fairly captured by most of the computational strategies. However, the comparisons reveal significant discrepancies regarding CO mass fraction prediction. Three causes may explain this phenomenon:

1. A higher sensitivity of carbon monoxide to the simplification of detailed chemistry, especially when multiple combustion regimes are encountered.
2. A bias introduced by artificial thickening, which overestimates the species mass production rate.
3. The influence of the subgrid scale flame wrinkling on the filtered chemical flame structure, which is challenging to model for intermediate species [66].

6. Acknowledgements

We are grateful for the opportunities provided by the TNF workshop (https://tnfworkshop.org). The simulations performed by EM2C-CNRS was granted access to the HPC resources from IDRIS, TGCC and CINES under the allocation A0052B10253 made by GENCI (Grand Equipement National de Calcul Intensif) and HPC resources from the Mesocentre computing center of CentraleSupelec and Ecole Normale Supérieure Paris-Saclay supported by CNRS and Région Ile-de-France (http:// mesocentre.centralesupelec.fr/). Vincent Moureau and Ghislain Lartigue from CORIA lab are acknowledged for providing the YALES2 code. The author from Jiangsu University acknowledges the support by the Natural Science Foundation of China (NSFC) under Grant No. 91741117. KTH simulations were performed on resources provided by the National Academic Infrastructure for Supercomputing in Sweden (NAISS) at NSC and PDC super-computing centers. The authors from TUDa acknowledge funding by the Deutsche Forschungsgemeinschaft (DFG, German Research Foundation) - Projektnummer 325144795. Work from ULB has received funding from the European Research Council (ERC) under the European Union's Horizon 2020 research and innovation programme under grant agreement No 714605 and Marie Skłodowska-Curie grant agreement No 801505. A. Péquin acknowledges the financial support of the Fonds National de la Recherche Scientifique (FRS-FNRS). J.C.M. and N.S. acknowledge the financial support from Mitsubishi Heavy Industries, Ltd., Takasago, Japan. Z.L. and N.S. acknowledge the financial support from the EPSRC (grant number EP/S025650/1). The work of Z.X.C. is supported by the NSFC (grant number 52276096) and the Emerging Interdisciplinary-

Young Scholars Project, Peking University, the Fundamental Research Funds for the Central Universities. This work used the ARCHER2 UK National Supercomputing Service (https://www.archer2.ac.uk). J.C.M., Z.L., Z.X.C and N.S. are grateful to the EPSRC (grant number EP/R029369/1) and ARCHER2 for financial and computational support as a part of their funding to the UK Consortium on Turbulent Reacting Flows (https://www.ukctrf.com).

group code	processors clock rate	N cores	T C-time	t sim-time	n cells	T/t	$T/t/n$ (CC)
–	–	1	10^3h	s	10^6	1	1
A YALES2 LM	AMD Rome 2.6 GHz	768	354	0.12	31	10 624	**343**
B O.FOAM C	AMD EPYC 7442 2.25 GHz	128	116	0.48	4.34	876	**202**
C O.FOAM C	16-core Intel Haswell, 2.3 GHz	1024	800	0.54	8	5300	**666**
D O.FOAM C	AMD EPYC 7742 2.25 GHz	1024	51	0.1	3.5	1 836	**524**
E O.FOAM LM	Xeon Platinum 817 3.1 GHz	1200	244	0.08	31	11 000	**354**
F O.FOAM LM	AMD EPYC 7742 3.4 GHz	128	72	0.4	1	648	**648**
G O.FOAM LM	Xeon 2680 2.7 GHz	108	9.7	0.04	3.87	872	**226**
H O.FOAM LM	Xeon E5-2603 1.6 GHz	240	73	0.11	3.5	2389	**682**
I PsiPhi LM	AMD EPYC 7742 1.6 GHz	65536	7000	0.4	2 200	63 000	**28**

Table 4: Overview of the computations. The table shows the research groups with code name (C: Compressible; LM: Low Mach) , the type of processors with its clock rate, the number of cores, the core-hours, the simulated real time, the number of grid cells, the ratio of core time to real time and finally the computational cost (CC) defined as the ratio of core time to real time per cell.

References

[1] A. Masri, Partial premixing and stratification in turbulent flames, Proc. Comb. Inst. 35 (2015) 1115–1136.

[2] T. Poinsot, D. Veynante, Theoritical and numerical combustion, RT Edwards, Inc., 2005.

[3] B. Fiorina, M. Cailler, Accounting for complex chemistry in the simulations of future turbulent combustion systems, in: AIAA Scitech 2019 Forum, 2019.

[4] T. Turányi, Reduction of large reaction mechanisms, New J. Chem 14 (1990) 795–803.

[5] P. Pepiot-Desjardins, H. Pitsch, An efficient error-propagation-based reduction method for large chemical kinetic mechanisms, Combust. Flame 154 (2008) 67–81.

[6] D. A. Goussis, U. Maas, Model reduction for combustion chemistry, in: Turbulent Combustion Modeling, Springer, 2011, pp. 193–220.

[7] T. Lu, C. K. Law, Systematic approach to obtain analytic solutions of quasi steady state species in reduced mechanisms, J. Phys. Chem. A 110 (2006) 13202–13208.

[8] U. Maas, S. B. Pope, Simplifying chemical kinetics: Intrinsic low-dimensional manifolds in composition space, Combust. Flame 88 (1992) 239 – 264.

[9] B. Fiorina, D. Veynante, S. Candel, Modeling combustion chemistry in large eddy simulation of turbulent flames, Flow. Turbul. Combust. 94 (2015) 3–42.

[10] J. van Oijen, Flamelet-Generated Manifolds: development and application to premixed laminar Flames, Ph.D. thesis, Technische Universiteit Eindhoven, 2002.

[11] O. Gicquel, N. Darabiha, D. Thévenin, Laminar premixed hydrogen / air counterflow flame simulations using flame prolongation of ILDM with differential diffusion, Proc. Comb. Inst. 28 (2000) 1901–1908.

[12] N. Peters, Laminar flamelet concepts in turbulent combustion, 21st Symposium (Int.) on Combustion, The Combustion Institute (1986) 1231–1250.

[13] C. D. Pierce, P. Moin, Progress-variable approach for large-eddy simulation of non-premixed turbulent combustion, J. Fluid Mech. 504 (2004) 73–97.

[14] B. Fiorina, O. Gicquel, L. Vervisch, S. Carpentier, N. Darabiha, Approximating the chemical structure of partially premixed and diffusion counterflow flames using FPI flamelet tabulation, Combust. Flame 140 (2005) 147–160.

[15] C. L. Westbrook, F. L. Dryer, Simplified reaction mechanisms for the oxidation of hydrocarbon fuels in flames, Combust. Sci. Technol. 27 (1981) 31–43.

[16] E. Fernández-Tarrazo, A. L. Sánchez, A. Liñán, F. A. Williams, A simple one-step chemistry model for partially premixed hydrocarbon combustion, Combust. Flame 147 (2006) 32–38.

[17] M. Cailler, N. Darabiha, B. Fiorina, Development of a virtual optimized chemistry method. application to hydrocarbon/air combustion, Combust. Flame 211 (2020) 281–302.

[18] D. Veynante, L. Vervisch, Turbulent combustion modeling, Prog. Energ. Combust. 28 (2002) 193 – 266.

[19] O. Colin, F. Ducros, D. Veynante, T. Poinsot, A thickened flame model for large eddy simulations of turbulent premixed combustion, Phys. Fluids 12 (2000) 1843–1863.

[20] B. Fiorina, R. Vicquelin, P. Auzillon, N. Darabiha, O. Gicquel, D. Veynante, A filtered tabulated chemistry model for LES of premixed combustion, Combust. Flame 157 (2010) 465 – 475.

[21] F. Charlette, C. Meneveau, D. Veynante, A power-law flame wrinkling model for les of premixed turbulent combustion, part i: non-dynamic formulation, Combust. Flame 131 (2002) 159–180.

[22] G. Wang, M. Boileau, D. Veynante, Implementation of a dynamic thickened flame model for large eddy simulations of turbulent premixed combustion, Combust. Flame 158 (2011) 2199 – 2213.

[23] D. Haworth, Progress in probability density function methods for turbulent reacting flows, Progress. Energ. Combust. 36 (2010) 168 – 259.

[24] A. Péquin, S. Iavarone, R. Malpica Galassi, A. Parente, The partially stirred reactor model for combustion closure in large eddy simulations: Physical principles, sub-models for the cell reacting fraction, and open challenges, Phys. Fluids 34 (2022) 055122.

[25] S. Iavarone, A. Péquin, Z. X. Chen, N. A. K. Doan, N. Swaminathan, A. Parente, An a priori assessment of the partially stirred reactor (PaSR) model for mild combustion, Proc. Comb. Inst. 38 (2021) 5403–5414.

[26] TNF Workshop, ????, International workshop on measurement and computation of turbulent flames.

[27] G. Kuenne, F. Seffrin, F. Fuest, T. Stahler, A. Ketelheun, D. Geyer, J. Janicka, A. Dreizler, Experimental and numerical analysis of a lean premixed stratified burner using 1D Raman/Rayleigh scattering and large eddy simulation, Combust. Flame 159 (2012) 2669–2689.

[28] B. Fiorina, R. Mercier, G. Kuenne, A. Ketelheun, A. Avdic, J. Janicka, D. Geyer, A. Dreizler, E. Alenius, C. Duwig, P. Trisjono, K. Kleinheinz, S. Kang, H. Pitsch, F. Proch, F. Cavallo Marincola, A. Kempf, Challenging modeling strategies for LES of non-adiabatic turbulent stratified combustion, Combust. Flame 162 (2015) 4264–4282.

[29] D. Butz, S. Hartl, S. Popp, S. Walther, R. S. Barlow, C. Hasse, A. Dreizler, D. Geyer, Local flame structure analysis in turbulent ch4/air flames with multi-regime characteristics, Combust. Flame 210 (2019) 426–438.

[30] S. Popp, S. Hartl, D. Butz, D. Geyer, A. Dreizler, L. Vervisch, C. Hasse, Assessing multi-regime combustion in a novel burner configuration with

large eddy simulations using tabulated chemistry, Proc. Combust. Inst. 38 (2021) 2551–2558.

[31] J. C. Massey, Z. Li, Z. X. Chen, Y. Tanaka, N. Swaminathan, Large eddy simulation of multi-regime combustion with a two-progress variable approach for carbon monoxide, Proc. Comb. Inst. (2022).

[32] D. Butz, A. Breicher, R. Barlow, D. Geyer, A. Dreizler, Turbulent multi-regime methane-air flames analysed by raman/rayleigh spectroscopy and conditional velocity field measurements, Combust. Flame 243 (2022) 111941. A dedication to Professor Katharina Kohse-Höinghaus.

[33] S. Hartl, D. Geyer, A. Dreizler, G. Magnotti, R. S. Barlow, C. Hasse, Regime identification from raman/rayleigh line measurements in partially premixed flames, Combust. Flame 189 (2018) 126–141.

[34] V. Moureau, P. Domingo, L. Vervisch, Design of a massively parallel CFD code for complex geometries, Cr. Mécanique 339 (2011) 141 – 148.

[35] A. Kempf, B. Geurts, J. Oefelein, Error analysis of large-eddy simulation of the turbulent non-premixed sydney bluff-body flame, Combust. Flame 158 (2011) 2408–2419.

[36] F. Ducros, F. Nicoud, T. Poinsot, Wall-adapting local eddy-viscosity models for simulations in complex geometries., in: B. M. J. (Ed.), ICFD, 1998, pp. 293–300.

[37] F. Nicoud, H. B. Toda, O. Cabrit, S. Bose, J. Lee, Using singular values to build a subgrid-scale model for large eddy simulations, Phys. Fluids 23 (2011) 085106.

[38] M. Germano, U. Piomelli, P. Moin, W. H. Cabot, A dynamic subgrid-scale eddy viscosity model, Phys. Fluids 3 (1991) 1760–1765.

[39] A. Yoshizawa, Statistical theory for compressible turbulent shear flows, with the application to subgrid modeling, Phys. Fluids 29 (1986) 2152–2164.

[40] J. Smagorinsky, General circulation experiments with the primitive equations i. the basic experiment., Mon. Weather Rev. 91 (1963) 99–164.

[41] J. A. van Oijen, L. P. H. de Goey, Modelling of premixed laminar flames using flamelet-generated manifolds, Combust. Sci. Technol. 161 (2000) 113–137.

[42] S. Delhaye, L. Somers, J. van Oijen, L. de Goey, Incorporating unsteady flow-effects in flamelet-generated manifolds, Combust. Flame 155 (2008) 133–144.

[43] L. Ma, X. Huang, D. Roekaerts, Large eddy simulation of co2 diluted oxy-fuel spray flames, Fuel 201 (2017) 165–175. 1st International Workshop on Oxy-Fuel Combustion.

[44] J. A. V. Oijen, A. Donini, R. J. M. Bastiaans, J. H. M. T. Boonkkamp, L. P. H. D. Goey, State-of-the-art in premixed combustion modeling using flamelet generated manifolds, Prog. Energ. Combust. 57 (2016) 30–74.

[45] K. Toshimitsu, A. Matsuo, M. R. Kamel, C. I. Morris, R. K. Hanson, Numerical simulations and planar laser-induced fluorescence imaging results of hypersonic reactive flows, J. Propul. Power 16 (2000) 16–21.

[46] I. S. Ertesvåg, B. F. Magnussen, The eddy dissipation turbulence energy cascade model, Combust. Sci. Technol. 159 (2000) 213–235.

[47] G. Gargiulo, P. Ciottoli, E. Martelli, R. M. Galassi, M. Valorani, Numerical analysis of laser-pulse transient ignition of oxygen/methane mixtures in rocket-like combustion chamber, Acta Astronaut. 159 (2019) 136–155.

[48] S. Ruan, N. Swaminathan, O. Darbyshire, Modelling of turbulent lifted jet flames using flamelets: a priori assessment and a posteriori validation, Combust. Theor. Model. 18 (2014) 295–329.

[49] Z. Chen, S. Ruan, N. Swaminathan, Large eddy simulation of flame edge evolution in a spark-ignited methane–air jet, Proc. Comb. Inst. 36 (2017) 1645–1652.

[50] J. C. Massey, Z. X. Chen, N. Swaminathan, Modelling heat loss effects in the large eddy simulation of a lean swirl-stabilised flame, Flow Turbul. Combust. 106 (2021) 1355–1378.

[51] V. Golovitchev, J. Chomiak, Numerical modeling of high temperature air flameless combustion, in: Proceedings of the 4th International Symposium on High Temperature Air Combustion and Gasification (HiTACG), 2001, pp. 761–774.

[52] K. Zhang, S. Dybe, Y. Z. Shen, S. Schimek, C. O. Paschereit, C. Duwig, Experimental and numerical investigation of ultra-wet methane combustion technique for power generation, in: Turbo Expo: Power for Land, Sea, and Air, ASME, 2021, pp. GT2020–16105.

[53] T. Lu, C. K. Law, Toward accommodating realistic fuel chemistry in large-scale computations, Prog. Energ. Combust. 35 (2009) 192–215.

[54] J. Floyd, A. M. Kempf, A. Kronenburg 1, R. Ram, A simple model for the filtered density function for passive scalar combustion LES, Combust. Theor. Model. 13 (2009) 559–588.

[55] A. Donini, R. Bastiaans, J. van Oijen, L. de Goey, A 5-D implementation of fgm for the large eddy simulation of a stratified swirled flame with heat loss in a gas turbine combustor, Flow Turbul. Combust. 98 (2017) 887–922.

[56] T. Lu, C. K. Law, A criterion based on computational singular perturbation for the identification of quasi steady state species: A reduced mechanism for methane oxidation with no chemistry, Combust. Flame 154 (2008) 761–774.

[57] S. Popp, Large Eddy Simulation of Turbulent Multi-Regime Combustion: Potentials and Limitations of Flamelet-Based Chemistry Modeling, Ph.D. thesis, Technische Universität Darmstadt, 2020.

[58] S. Nambully, P. Domingo, V. Moureau, L. Vervisch, A filtered-laminar-flame PDF sub-grid scale closure for LES of premixed turbulent flames. part I: Formalism and application to a bluff-body burner with differential diffusion, Combustion and Flame 161 (2014) 1756–1774.

[59] S. Nambully, P. Domingo, V. Moureau, L. Vervisch, A filtered-laminar-flame PDF sub-grid-scale closure for LES of premixed turbulent flames.

part II: Application to a stratified bluff-body burner, Combustion and Flame 161 (2014) 1775–1791.

[60] W. Zhang, S. Karaca, J. Wang, Z. Huang, J. van Oijen, Large eddy simulation of the cambridge/sandia stratified flame with flamelet-generated manifolds: Effects of non-unity lewis numbers and stretch, Combust. Flame 227 (2021) 106–119.

[61] L. Engelmann, P. Wollny, A. Breicher, D. Geyer, N. Chakraborty, A. Kempf, Numerical analysis of multi-regime combustion using flamelet generated manifolds - a highly-resolved large-eddy simulation of the darmstadt multi-regime burner, Combustion and Flame 251 (2023) 112718. URL: https://www.sciencedirect.com/science/article/pii/S0010218023001037. doi:https://doi.org/10.1016/j.combustflame.2023.112718.

[62] P. Gruhlke, E. Inanc, R. Mercier, B. Fiorina, A. M. Kempf, A simple post-processing method to correct species predictions in artificially thickened turbulent flames, Proc. Combust. Inst. 38 (2021) 2977–2984.

[63] G. Maio, M. Cailler, R. Mercier, B. Fiorina, Virtual chemistry for temperature and CO prediction in LES of non-adiabatic turbulent flames, Proc. Combust. Inst. 37 (2019) 2591–2599.

[64] P. Benard, G. Lartigue, V. Moureau, R. Mercier, Large-eddy simulation of the lean-premixed preccinsta burner with wall heat loss, Proc. Comb. Inst. 37 (2019) 5233–5243.

[65] L. Vervisch, P. Domingo, G. Lodato, D. Veynante, Scalar energy fluctuations in large-eddy simulation of turbulent flames: Statistical budgets and mesh quality criterion, Combust. Flame 157 (2010) 778–789.

[66] R. Mercier, C. Mehl, B. Fiorina, V. Moureau, Filtered wrinkled flamelets model for large-eddy simulation of turbulent premixed combustion, Combust. Flame 205 (2019) 93–108.

[67] V. Moureau, P. Domingo, L. Vervisch, From large-eddy simulation to direct numerical simulation of a lean premixed swirl flame: Filtered laminar flame-PDF modeling, Combustion and Flame 158 (2011) 1340 – 1357.

[68] P. Auzillon, B. Fiorina, R. Vicquelin, N. Darabiha, O. Gicquel, D. Veynante, Modeling chemical flame structure and combustion dynamics in LES, Proc. Combust. Inst. 33 (2011) 1331 – 1338.

[69] R. M. Dudley, Probabilities and metrics: Convergence of laws on metric spaces, with a view to statistical testing, volume 45, Aarhus Universitet, Matematisk Institut, 1976.

[70] O. Pele, M. Werman, Fast and robust earth mover's distances, in: 2009 IEEE 12th International Conference on Computer Vision, IEEE, 2009, pp. 460–467.

[71] R. Johnson, H. Wu, M. Ihme, A general probabilistic approach for the quantitative assessment of les combustion models, Combust. Flame 183 (2017) 88–101.

[72] G. Maio, M. Cailler, N. Darabiha, B. Fiorina, Capturing multi-regime combustion in turbulent flames with a virtual chemistry approach, Proc. Combust. Inst. 38 (2021) 2559–2569. URL: https://www.sciencedirect.com/science/article/pii/S1540748920302054. doi:https://doi.org/10.1016/j.proci.2020.06.131.